Arrays of TiO₂ nanorods embedded with fluorine doped carbon nitride quantum dots (CNFQDs) for visible light driven water splitting

Pawan Kumar,[1‡] Ujwal Thakur,[1‡] Kazi Alam,[1] Ryan Kisslinger,[1] Sheng Zeng,[1] Sahil Patel[1] Piyush Kar[1] and Karthik Shankar[1,2]*

[1]*Department of Electrical and Computer Engineering, University of Alberta, 9211 - 116 St, Edmonton, Alberta, Canada T6G 1H9*

[2] *NRC National Institute for Nanotechnology, 11421 Saskatchewan Dr NW, Edmonton, AB T6G 2M9, Canada*

‡These authors contributed equally

†Electronic supplementary information (ESI) available. See DOI:

Abstract

Graphenic semiconductors such as carbon nitride are attracting increasing attention as photocatalysts due to their chemical stability, visible light absorption and excellent electronic properties. The photocatalytic activity of nanostructured TiO_2 catalysts is constrained by the wide bandgap and concomitant low visible light responsivity of TiO_2. In this context we present the formation of new fluorine doped carbon nitride quantum dots (CNFQDs) by solid state reaction and the subsequent examination of their heterojunctions with TiO_2 for photoelectrochemical water splitting. Arrays of rutile phase TiO_2 nanorods embedded with CNFQDs were synthesized by a simple *in situ* hydrothermal approach and the resulting nanomaterials were found to exhibit strong visible light absorption. The energetics at the heterojunction were favorable for efficient electron transfer from CNFQDs to TiO_2 under visible light irradiation and transfer of holes to the aqueous electrolyte. CNFQD-sensitized TiO_2 nanorods exhibited a strong photoelectrochemical response up to 500 nm. Reuse experiments confirmed robustness and long term stability of the sample without exhausting the catalytic performance. The present work demonstrates a new pathway to sensitize TiO_2 to visible photons by the *in situ* formation of embedded heterojunctions with fluorine doped carbon nitride quantum dots.

KEYWORDS:, Hydrogen Generation, Quantum Confinement, Semiconductor Photoelectrocatalysis, Water Splitting, Metal-Free Catalysts, Nanowires.

1. Introduction

The energy crisis due to depletion of fossil fuel reserves and alarming environmental pollution has triggered research to search for alternative, clean and sustainable energy resources [1, 2]. Photoelectrochemical water splitting to produce hydrogen using visible light and applied bias has

wide potential to solve these problems due to the high free energy content of H_2 (ΔG = +237 kJ mol^{-1}), a nearly inexhaustible supply of resources *ie:* water and sunlight, and the generation of water as the sole by-product following combustion [3-5]. Due to energy constraints, water splitting requires a photocatalyst which can reduce the activation energy barrier by supplying electrons and holes to reduce hydrogen and oxidize water. In search of the ideal visible light active photocatalyst, numerous semiconductor materials have been explored but most of them suffer from one or more debilitating drawbacks such as a lack of visible light absorption, a lack of photostability or a low catalytic quantum efficiency [6].

In recent years, carbon quantum dots (CQDs) which are sp^2 and sp^3 hybridized graphitic or turbostatic quasispherical carbon nanoparticles have proven to be excellent electronic materials for photocatalysis, catalysis, sensing and OLEDs due to facile synthesis, small band gap, intense photoluminescence (following surface passivation), and size and surface tunability of optoelectronic properties [7]. Carbon nitride quantum dots (CNQDs), nitrogen rich descendents of the carbon nitride frame work composed of a tris-*s*-triazine skeleton, are gaining popularity over CQDs due to their higher chemical and photostability, easy synthesis and brighter fluorescence [8-11]. Doping with heteroatoms (N, S, O *etc*) and surface functionalization can further improve the fluorescence intensity, carrier lifetime, and photocatalytic behaviour of CNQDs [12]. For instance, Lu *et al* prepared S and O co-doped CNQDs using thiourea and citric acid which exhibited excellent performance for mercury detection and cell imaging [13]. Interestingly fluorine doping in carbon nitride can distort the symmetry of some conjugated domains, in turn altering the band gap and band edge positions to improve photocatalytic performance [14]. Wang *et al* demonstrated the synthesis of F doped carbon nitride quantum dots (F–C_3N_4) of size range 1.5–2.0 nm by

fragmentation of bulk sheets in ethylene glycol under ultrasonication treatment which exhibited excellent PL quantum yields (39.03%) [15].

TiO$_2$ is the most studied semiconductor photocatalyst due to its high catalytic activity, non-toxic nature, chemical and photocorrosion resistance, and wide abundance. However, TiO$_2$'s wide band gap and less reductive conduction band constitute the key obstacles limiting performance [16]. Doping or decorating TiO$_2$ with noble metals (Au, Ag, Ru, Pd, Cu, Pt, CuPt, *etc*) [17-21], doping with non-metals (C, N, S, F, *etc*) [22-26], sensitization with various molecular complexes (Ru, Ir, Pt, Re complexes) [27-29], composite formation with low band gap semiconductors [30, 31], and defect creation [32, 33] have been employed to increase visible light absorption, enhance charge separation and lengthen the carrier lifetime. Yet, the quantum efficiencies of TiO$_2$-based photocatalysts for visible photons remain too low, preventing the scale-up of the technology [34] [7, 35, 36]. Photoelectrochemical cells in which the photoanode is a sintered film of colloidal nanoparticles suffer from significant transport and recombination losses due to the random-walk nature of charge migration in such films [37]. One dimensional structures such as vertically oriented arrays of monocrystalline TiO$_2$ nanorods offer continuous vectorial percolation pathways and improved charge transport owing to a more ordered structural and crystalline feature [38-46], which motivated us to use TiO$_2$ nanowires as scaffolds for CNQDs.

Due to their lower band gap and aromatic π-conjugated framework, carbon nitride quantum dots can play the dual role of 1) photosensitizer – i.e. can donate electron to another system after absorption of light and 2) electron sink - can uptake electrons from another system to facilitate charge separation. To exploit this behavior, CNQD-decorated semiconductors photocatalysts have been reported. Pan *et al* [47] and Su *et al* [48] prepared CNQD-decorated TiO$_2$ nanotubes for enhanced activity for dye photodegradation. In another report Su *et al* formed TiO$_2$ nanotube arrays

(TNTAs) decorated with ultrasmall CNQDs which then showed a three fold increase in photocurrent compared to the TNTAs alone, in photoelectrochemical water splitting experiments [49]. Although the the photocatalytic performance increased upon decoration of CNQDs on TNTAs nanostructures, severe leaching of the CNQDs from the semiconductor surface and the resulting photocorrosion limits their practical usability. *In situ* growth of semiconductor materials in the presence of quantum dot sensitizers can lead to the formation of embedded nanostructures possessing enhanced robustness and reusability while maintaining similar photoactivity [50-52]. For example, *in situ* synthesized C_3N_4-CdS nanocomposite prepared by precipitation–deposition method showed excellent activity for the degradation of 4-aminobenzoic acid [53]. Similarly graphitic-C_3N_4 nanosheet hybridized N-doped TiO_2 nanofibers synthesized by an *in situ* approach afforded increased H_2 production and degradation [54]. Inspired by these studies, we synthesized fluorine doped carbon nitride quantum dots (CNFQDs) embedded in TiO_2 nanorods (CNF:TNR) by the *in situ* growth of TiO_2 nanorods in the presence of CNFQDs. The synthesized CNF:TNR photocatalyst materials exhibited excellent photoelectrochemical performance, robustness and reusability.

2. Results and discussion

2.1 Morphology, Structure and Composition of CNF:TNR nanocomposites

The fluorescent fluorine doped carbon nitride quantum dots (CNFQDs) were prepared by modifying a procedure previous reported for the synthesis of carbon nitride quantum dots.[55] The CNFQDs were synthesized by the solid state reaction of urea and citric acid (which serve as sources for the formation of the carbon nitride skeleton) and ammonium fluoride (which provides the fluorine dopant) at 200 ℃ in a Teflon autoclave (Fig. 1a). The *in situ* synthesis of CNFQDs embedded TiO_2 nanorods (CNF:TNR) was performed by hydrothermal treatment of titanium (IV)

butoxide in the presence of acetic acid, HCl and an aqueous suspension of CNFQDs at 200 °C, and a schematic illustration of this *in situ* process is shown in Fig. 1b.
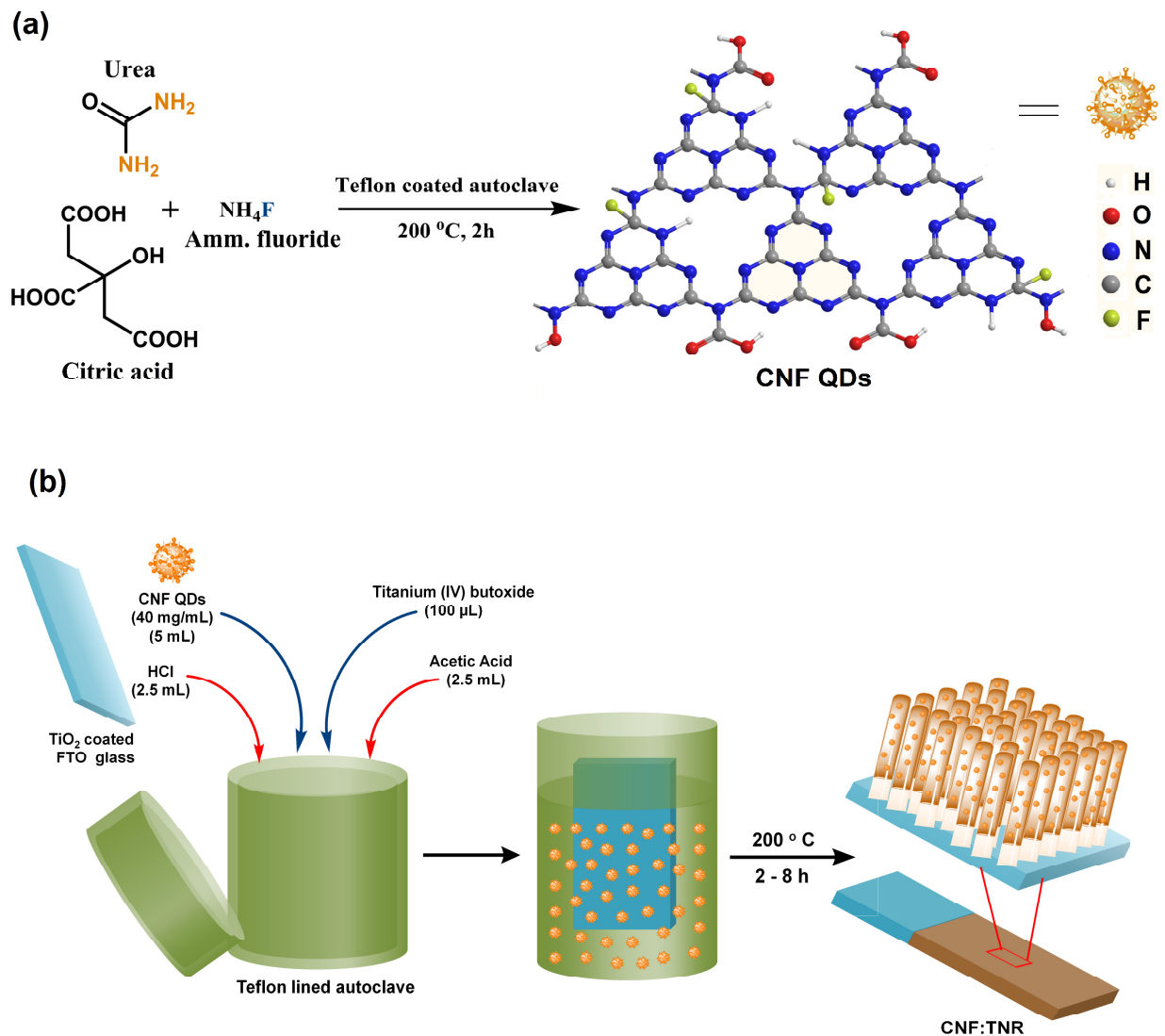
(a)

(b)

Figure 1. (a) Schematic of synthesis of CNFQDs and (b) Illustration of the formation process of CNF:TNR photocatalyst samples.
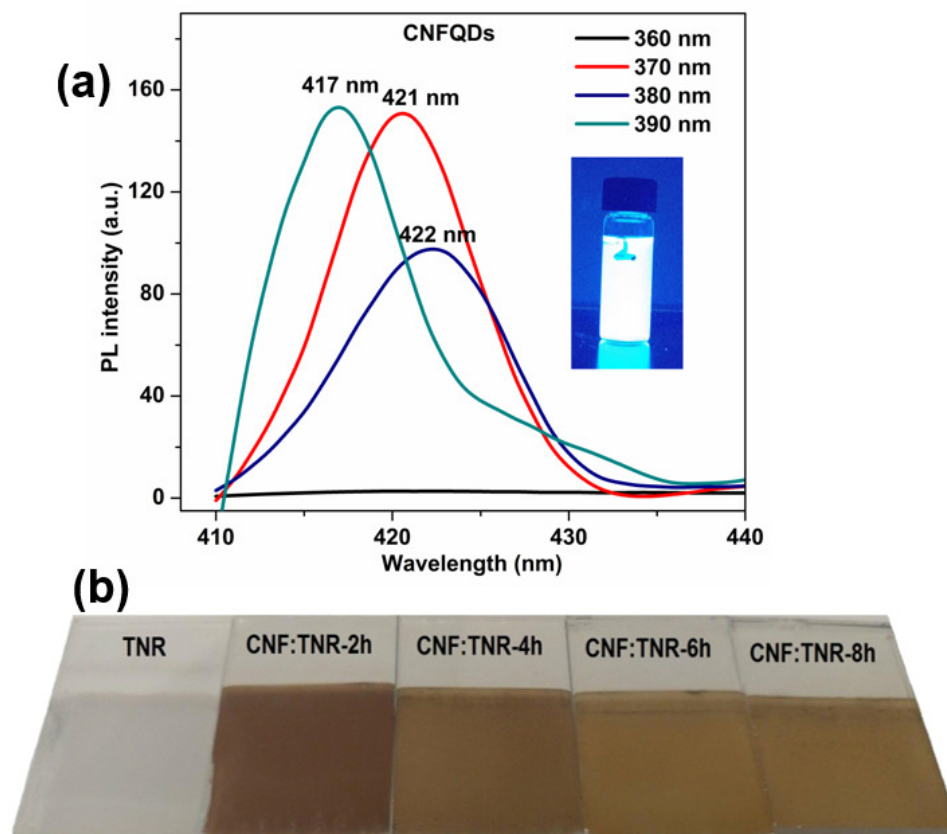
Figure 2. (a) PL spectra of CNFQDs excited at 360 nm (black), 370 nm (red), 380 nm (navy) and 390 nm (dark cyan) with Inset showing the fluorescence of a CNFQD suspension under UV light irradiation and (b) Photographs of TNR and CNF:TNR samples prepared using different durations of the hydrothermal formation process.

The obtained CNFQDs exhibited a bright blue fluorescence under UV light as seen in the Inset of Fig. 2a. The PL spectra (Fig. 2a) illustrate the excitation dependent emission behavior of of prepared CNFQDs wherein the emission peaks are red shifted from 417 nm to 422 nm as the excitation wavelength is changed from 370 nm to 390 nm, in line with previous reports on carbon nitride quantum dots [15, 56, 57]. The average particle size of the CNFQDs was found to be 7 nm as determined from dynamic light scattering (DLS) (Fig. S1) and the associated average zeta potential (surface charge) was calculated to be −21.3 mV (Fig. S2), which is attributed to amine

and carboxylate groups on the surface of the quantum dots [55]. Various CNF:TNR samples were prepared by maintaining reaction times of 2, 4, 6 and 8 h, and are denoted by CNF:TNR-2h, CNF:TNR-4h, CNF:TNR-6h and CNF:TNR-8h respectively. During hydrothermal growth of TiO_2 nanorods (TNRs), the fluorinated carbon nitride quantum dots get partially embedded in the nanorods. The embedding of the CNFQDs in the nanorods was inferred from Raman, infrared and photoelectron spectra (shown and analyzed later) as well as from the leaching characteristics of the samples. CNFQDs are very soluble in KOH and surface adsorbed carbon nitride quantum dots are known to leach out by KOH treatment; however *in situ* CNF:TNR samples did not show the slightest leaching even after repeated cycling in KOH. We attribute the embedding of the quantum dots in the TNR framework to the interaction of the active suface groups on the CNFQDs with the exposed facets of growing rutile crystallites. The embedded nature of the quantum dots provides robustness and stability to the CNFQDs/TNR composite, and also enables the absorption of visible light. Due to the entrapment of CNFQDs in the TNR structure, the color of the samples turns to dark brown as seen in Fig. 2b with the deepest color obtained for a reaction time of 2h. However no significant change in colour was observed upon increasing reaction time (Fig. 2b). CNF:TNR samples hydrothermally grown on FTO for reaction times longer than *ca* 12 h delaminated from the underlying FTO coated glass substrate.

The morphologies and size parameters of TNRs and CNF:TNR samples were determined using a field emission scanning electron microscope (FESEM). The FESEM top view of bare TNR samples grown after 2 h hydrothermal treatment exhibits evenly distributed TiO_2 nanorod on FTO substrate with blunt ends (Figs. 3a and 3c) while the cross sections indicate a mean nanorod length of ~ 1.0 µm and a near identical thickness throughout (Fig. 3e). The top view of the CNF:TNR-4h sample in SEM images show multidirectional well distributed nanorod clusters having slightly

pointed ends (Figs. 3b and 3d). The change in morphological character to unsymmetrical pointed nanorods occurs due to the intercalation of CNFQDs in the rutile crystal structure during the growth process which disturbs the TNR growth pattern. The average length of CNF:TNR-4h nanorods was found to be ~ 1.0 µm (Fig. 3f).
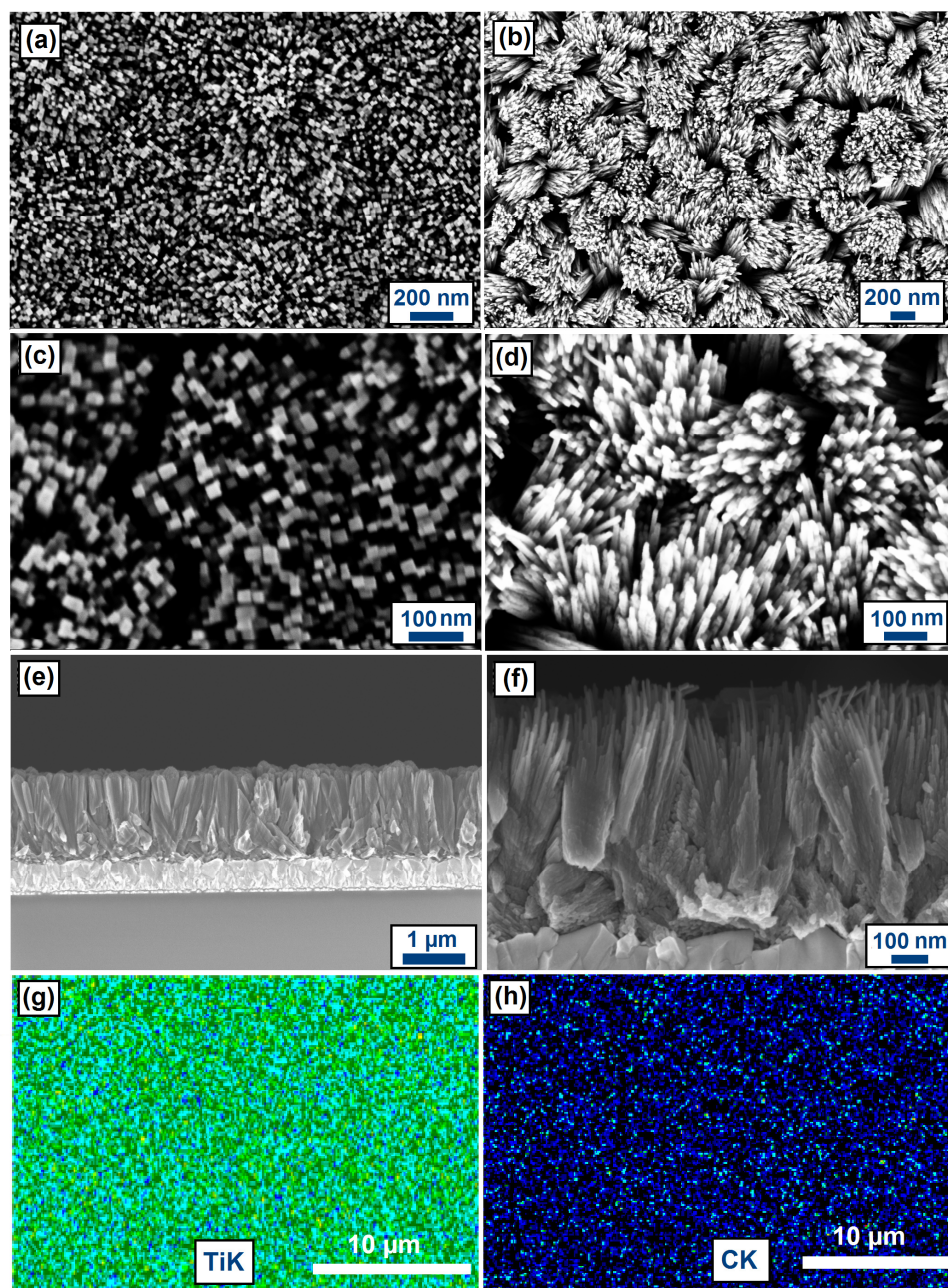
Figure 3. FESEM images of (a)(c)(e) TNR samples, and (b)(d)(f) *insitu* synthesized CNF:TNR-4h samples at 200 nm, 100 nm and cross section at 100 nm scale bar respectively.

The SEM images of the CNF:TNR-2h, CNF:TNR-6h and CNF:TNR-8h samples also reveal similar morphological geometry while the average length was found to be ~ 0.75 µm, 1.4 µm and 1.5 µm respectively (Fig. S5). The SEM elemental mapping of CNF:TNR-4h sample indicates the carbon to be evenly distributed in the CNF:TNR nanocomposite (Figs. 3g and 3h). A very small amount of fluorine was detected in the EDS spectrum of CNF:TNR composite (Fig. S4) which is indicative of a low atomic concentration.

The fine structural features of CNF:TNR-4h samples were determined using high resolution transmission electron microscopy (HRTEM) (Fig. 4). The TEM image of the CNF:TNR-4h sample clearly shows a monocrystalline nanorod having a width of 10 to 15 nm with discernible lattice finges whose interplanar d spacing of 0.27 nm corresponds to the 101 plane of rutile TiO_2 (Fig. 4a). Another TEM image of CNF:TNR-4h shows a nanorod with a d spacing 0.36 nm corresponding to the 110 plane of rutile TiO_2 (Figure 4b). These data are consistent with tetragonal rutile phase TiO_2 (JCPDS# 21-1276). The CNFQDs were not detected in HRTEM images most probably due to intercalation in the lattice structure and small size. Furthermore, complete dispersion of amorphous CNFQDs in the CNF:TNR composite prevents long range π-π stacking of CNFQDs, and the plane associated with CNFQDs cannot be observed in HRTEM, consistent with XRD of CNF:TNR samples where the peak associated with the 002 plane of carbon at a 2θ value of *c.a.* 26° was not detectable (Fig. 6a).
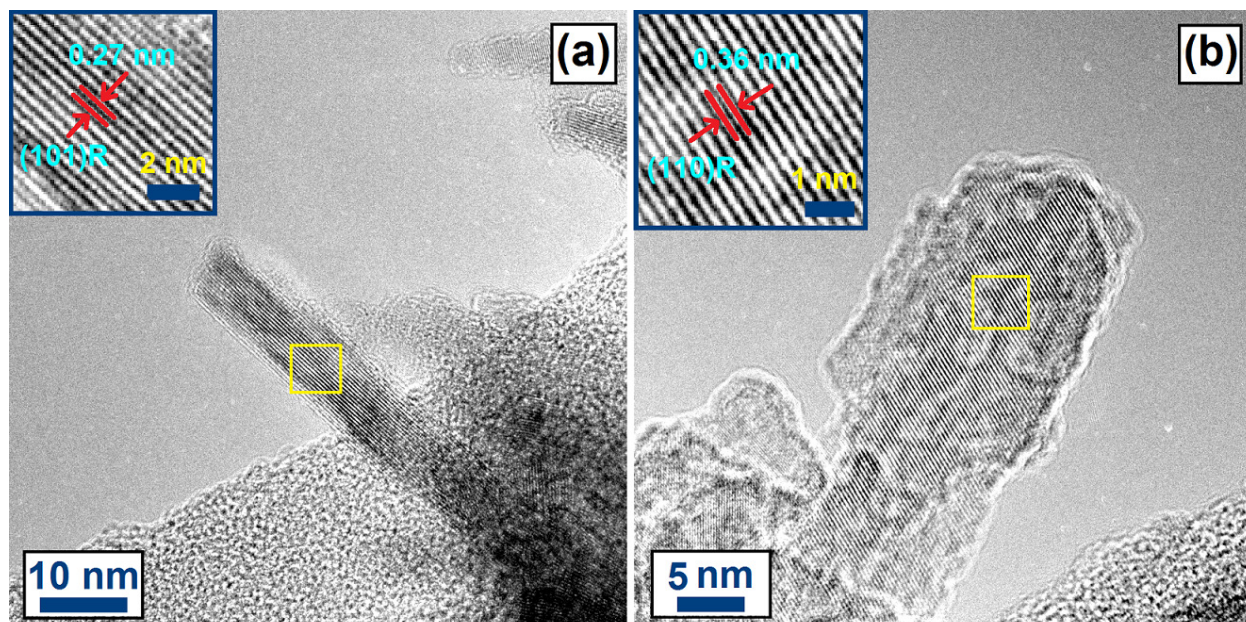
Figure 4. HR-TEM images of CNF:TNR-4h photocatalyst (a) at 10 nm and (b) at 5 nm scale bar; Insets showing interplanar *d* spacing at 1 nm scale bar.

FTIR spectra of CNFQDs, bare TNR samples and bare CNF samples are shown in Figs. 5a and 5b. The FTIR spectra of CNFQDs exhibit two peaks at 3438 cm^{-1} and 3335 cm^{-1} respectively due to the symmetric and asymmetric N–H stretching vibrations. The IR absorption band at 1680 cm^{-1} originated due to the cumulative bending vibrations of adsorbed H_2O and C=O stretches. Further, the peaks observed at 1584, 1466 and 1392-1068 cm^{-1} were assigned to C=N, C–N stretches and triazine ring (C_3N_3) deformations respectively [58, 59]. The FTIR spectrum of bare TNRs shows specific Ti–O stretch at 502 cm^{-1} and a broad hump around 3180 cm^{-1} due to O–H stretch. The FTIR spectra of all CNF:TNR samples show the characteristic peaks of TiO_2 at 501 cm^{-1} corresponding to Ti–O stretch. The presence of peaks due to C=N, C–N and C_3N_3 ring skeleton vibrations validates the presence of CNFQDs in the CNF:TNR composite.
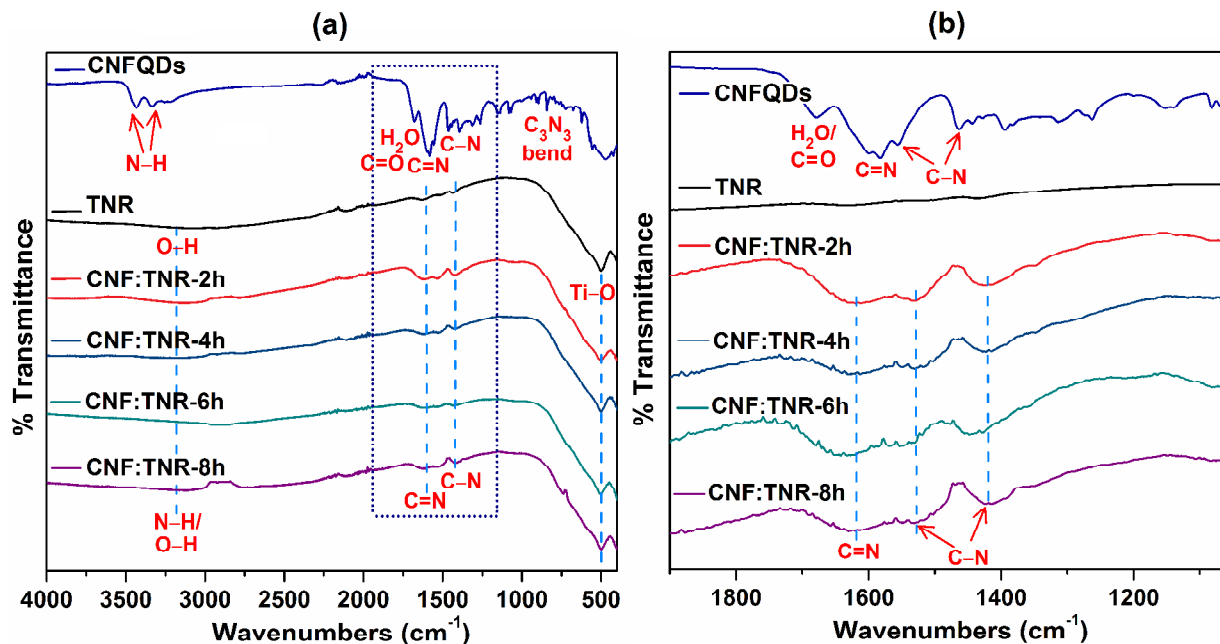
Figure 5. (a) Full range FTIR spectra of CNFQDs (blue), TNR (black), CNF:TNR samples prepared at 2h (red), 4h (navy blue), 6h (teak) and 8h (purple) time interval; (b) expanded in 1050-1900 cm^{-1} spectral region.

The structure of the synthesized nanocomposite materials was examined using X-ray diffraction (Fig. 6a). The XRD spectra of bare TNRs show diffraction peaks at 2θ values of 26.5º, 33.7º, 36.0º, 37.6º, 51.5º, 54.4º, 61.5º, 62.8º and 65.5º corresponding to (110), (101), (111), (210), (211), (220), (002), (310) and (301) crystal planes of tetragonal rutile phase TiO_2 respectively with the space group *P*4/*mnm* which was in well agreement with JCPDS file #21-1276 and previously published reports [60]. The absence of any peak for anatase TiO_2 clearly indicates the phase purity of the TNR samples. The XRD diffraction pattern of CNF:TNR was found to be identical to bare TNR sample showing that the *in situ* introduction of CNFQDs in TiO_2 nanorods does not change the crystalline nature of the nanorods. The absence of any broad XRD signal due to the 002 reflection of carbon suggests non-stacked CNFQDs that are well distributed in the TiO_2 matrix.

The presence of CNFQDs in the CNF:TNR structure and rutile phase was confirmed with Raman spectroscopy (Fig. 6b). The Raman spectrum of bare TiO_2 nanorods has characteristic

bands at 118, 442 and 613 cm^{-1} indexed to the B_{1g}, E_g and $A1_g$ active mode vibrations of tetragonal rutile phase TiO_2 [61, 62]. In addition a weak vibration band around 238 cm^{-1} was observed due to multiphon processes [63]. The Raman spectra of CNF:TNR samples exhibit all the vibrational peaks corresponding to rutile phase TiO_2. Additionally two characteristic features, namely the D and G bands specific to graphitic carbon materials were clearly observable at 1371 cm^{-1} and 1590 cm^{-1} which confirmed the presence of CNFQDs in the CNF:TNR samples [64]. The D band represents defects in the graphitic carbon nitride framework due to out of plane vibrations of sp^3 carbons while the G band specific to the graphitic structure originates due to in-plane vibrations of sp^2 carbons in the aromatic framework [65]. The D and G bands of the CNF:TNR-2h sample were quite weak; however as the reaction time was increased to 4 h, the intensity of the D and G bands in the Raman spectra increased significantly indicating better incorporation of the CNFQDs in TNR structure during the growth process and is also held to be responsible for the higher photocatalytic performance of the CNF:TNR-4h sample (see Section 2.4). However, further increment of reaction time to 6 and 8 h respectively did not significantly increase the Raman intensity of the D and G bands which might be due to reaching the maximum CNFQD concentration that TiO_2 nanorods can accommodate.
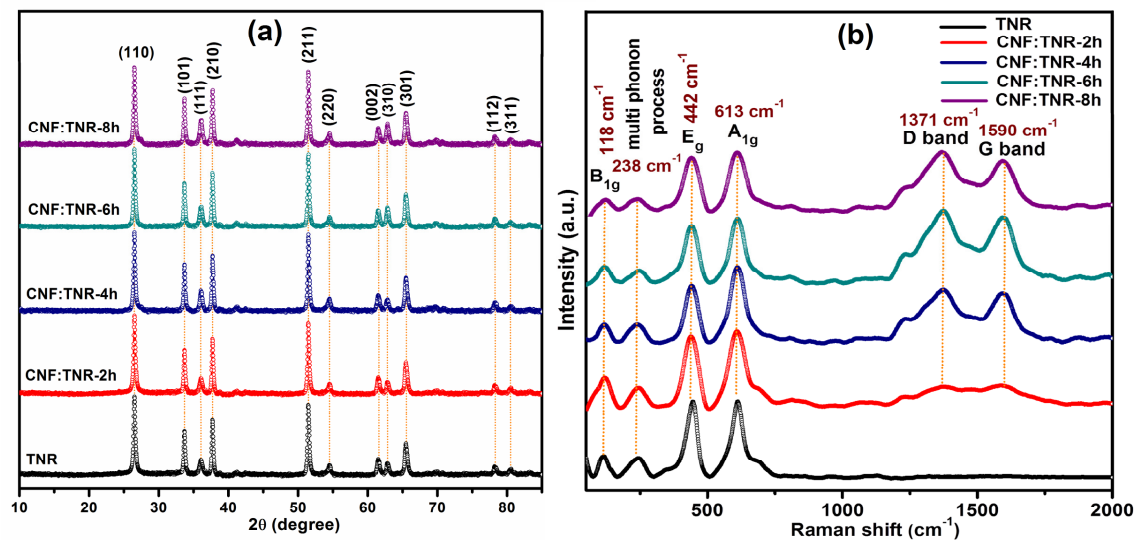
Figure 6. (a) X-ray diffraction (XRD) patterns and (b) Raman spectra of TNR (black), CNF:TNR samples synthesized at 2h (red), 4h (navy blue), 6h (dark cyan) and 8h (purple) time intervals.

The surface chemical composition, oxidation state and binding energy of the nanocomposite materials were determined using X-ray photoelectron spectroscopy (Fig. 7). The XPS elemental survey scan of CNF:TNR-4h revealed peaks due to the presence of C1s, N1s, O1s, Ti2p, and F1s core level spectra, and confirmed the existence of CNFQDs in the nanorod structure (Fig. S3a). The high resolution XPS spectra in the C1s region can be deconvolved into three peak components at binding energy 289.0, 286.7 and 284.9 eV due to N=C–N$_2$, N–C–N and C–C type of carbons [66]. The sp^2 carbon in N=C–N$_2$ and sp^3 carbon in N–C–N type carbons constitute the graphitic carbon nitride framework while sp^3 C–C carbon peaks occur due to the presence of the carboxylic group and turbostratic carbon in CNFQDs (Fig. 7a). Following deconvolution, the XPS spectra in the N1s region gave two peak components at binding energy values of 402.3 eV and 400.6 eV due to tertiary N–(C)$_3$ and secondary C=N–C nitrogens respectively (Fig. 7b) [67, 68]. The XPS spectra in the O1s region consists of three peak components at 533.7, 532.0 and 530.4 eV due to C=O, –OH and Ti–O oxygens (Fig. 7c). The two peak components at 464.2 eV and

458.3 eV in Ti2p region were assigned to Ti $2p_{1/2}$ and Ti $2p_{3/2}$ which corroborate the Ti^{4+} oxidation state of titanium in rutile TiO_2 (Fig. S3b) [69]. The XPS peak in the F1s region at 688.7 eV is due to carbon bonded fluorine (C–F) atoms and confirms fluorine doping of the carbon nitride quantum dots (Fig. 7d) [14, 15].
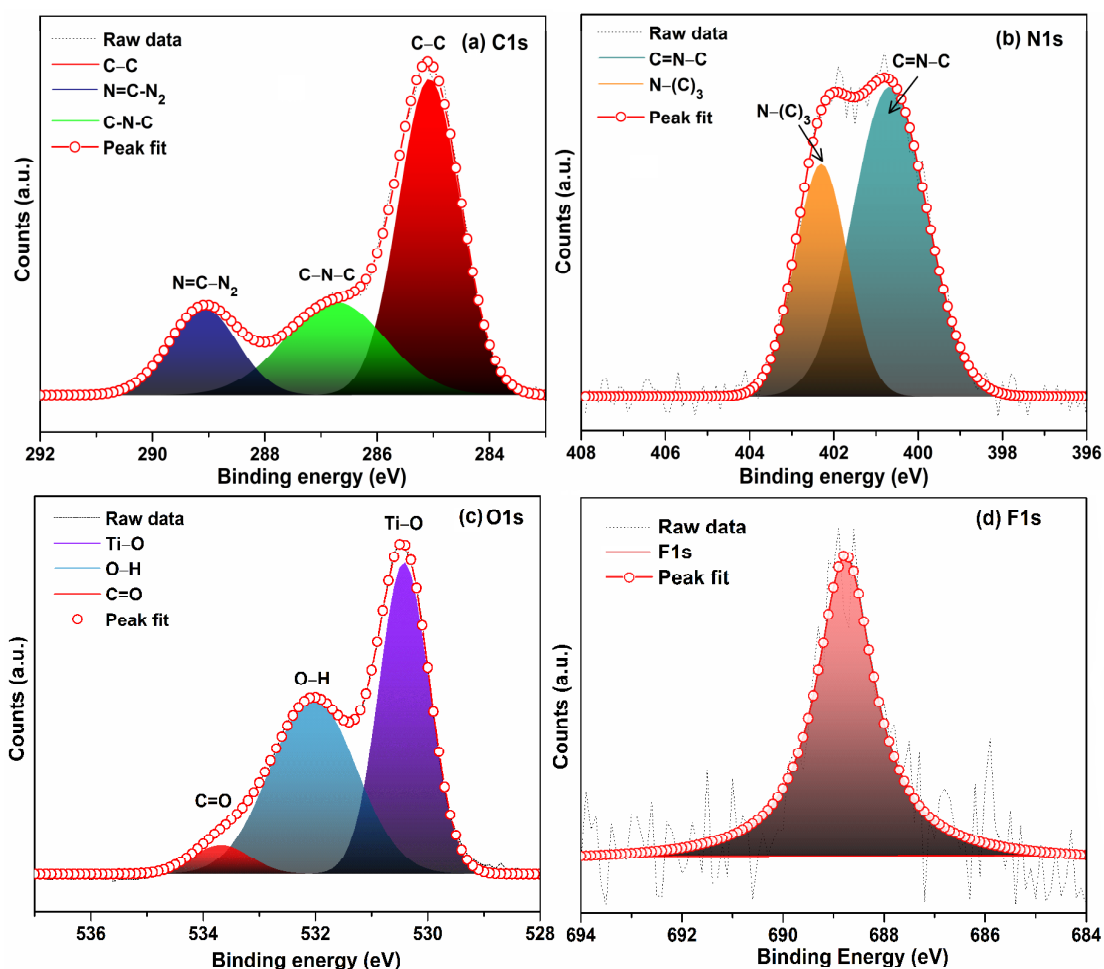

Figure 7. High resolution XPS spectra of CNF:TNR-4h showing (a) C1s, (b) N1s, (c) O1s and (d) F1s regions.

2.2 Optoelectronic properties of CNF:TNR nanocomposites

The optical absorption of the samples was quantified by UV-Vis diffuse reflectance spectroscopy (DRS), shown in Fig. 8a. The DRS spectra of TiO_2 nanorods (black curve in Fig. 8a) display a typical absorption band in the ultraviolet with a band edge at ~ 407 nm. Incorporation of CNFQDs

in the TiO$_2$ nanorod structure via the *in situ* hydrothermal process makes the resulting nanocomposite a visible light absorber; all the CNF:TNR samples show an increase in the absorption intensity in the visible region with a broad band tail extending to 700 nm.
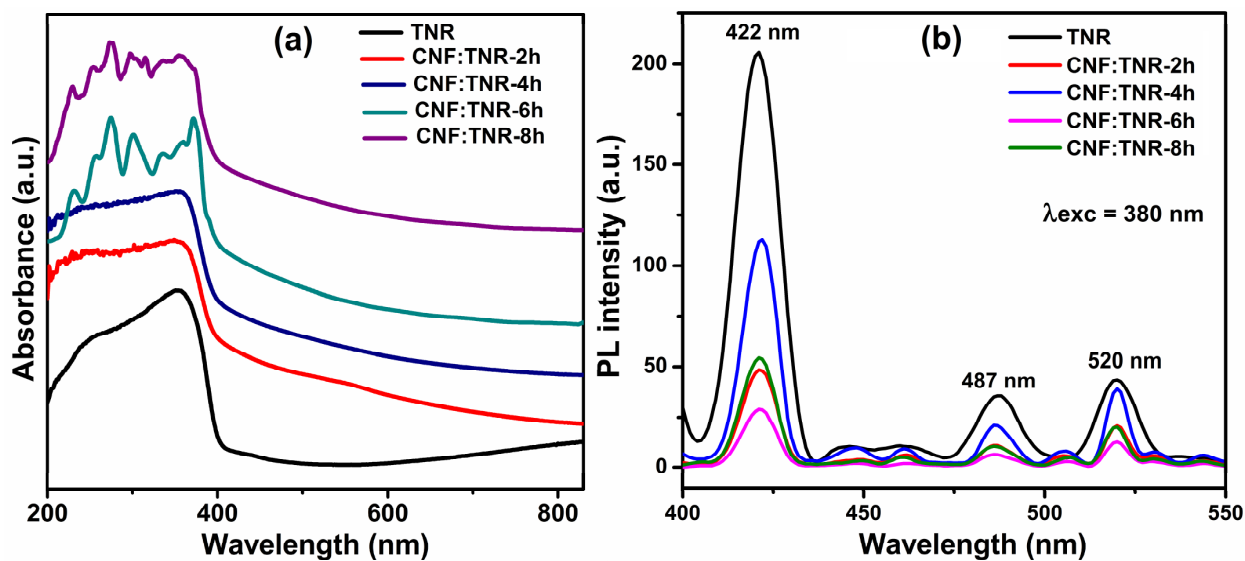

Figure 8. (a) UV-Vis diffuse reflectance spectra and (b) PL spectra of TNR(Black), CNF:TNR-2h (red), CNF:TNR-4h (navy blue), CNF:TNR-6h (dark cyan), CNF:TNR-8h (purple).
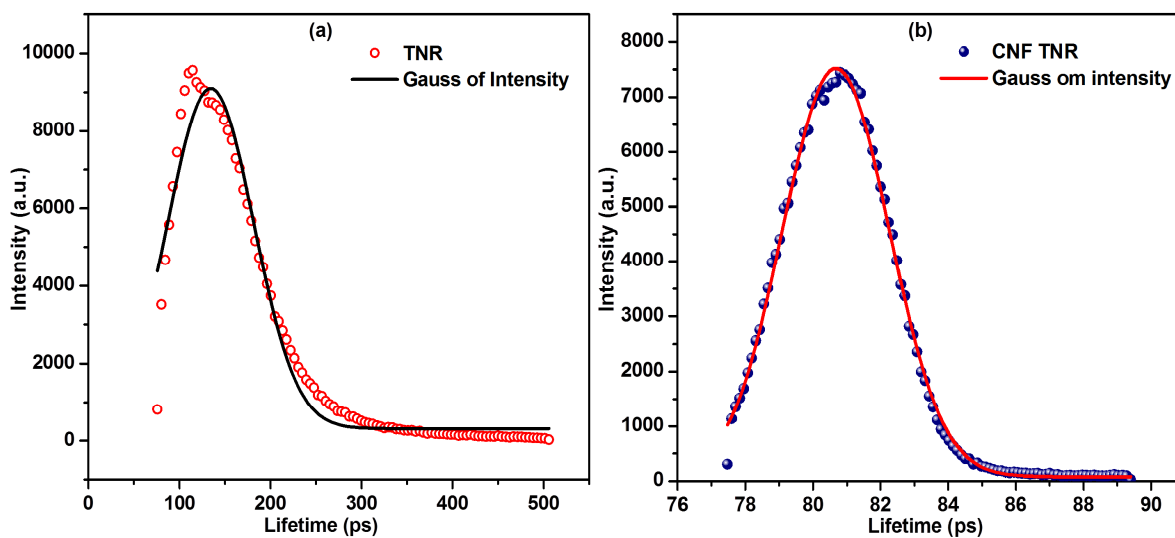

Figure 9. Time-resolved photoluminescence plots of (a) TNR and (b) CNF:TNR-4h.

The steady-state photoluminesence spectra of TNR and CNF:TNR samples are shown in Fig. 8b. To measure the PL spectra we chose an excitation wavelength of 380 nm because CNFQDs exhibit the highest PL intensity when excited at this wavelength, which represents the maximum generation of electron hole pairs. The PL spectra of bare TNR sample gave three peaks at 422, 487 and 529 nm for rutile phase TiO_2 which are in close proximity to previously reported values [70, 71]. The near band-edge emission peak at 422 nm is the dominant feature in the PL spectrum of rutile single crystals and was attributed to the one phonon replica of the 1s quadrupolar exciton [72]. The PL intensities of the three peaks decreased compared to the bare TNRs for each of the CNF:TNR samples, indicating partial quenching of the rutile photoluminescence due to the addition of CNFQDs in the TNR structure. The phenomenon of decrease in PL intensity can be explained due to hole transfer from the TiO_2 to the CNFQDs, preventing radiative recombination of the geminate electron hole pair. This inference of efficient charge transfer between the TiO_2 and the CNFQDs is also supported by the decrease in the PL lifetime of CNF:TNR samples compared to the bare TNR samples. Fig. 9 shows the time-resolved fluorescence decay curves of TNR and CNF:TNR samples excited by a two-photon femtosecond pulse laser at 750 nm with the emission window set between 341 nm and 704 nm. The two photon excitation using longer wavelength incident light ensures uniform excitation of the entire volume of the CNFQD-embedded nanorods and minimizes interference from surrounding species and Raman scattering, making it more advantageous than one photon excitation. The average PL lifetimes of the TNR and CNF:TNR samples were found to be 500 ps and 89 ps respectively.

The very weak PL emission from the CNF:TNR samples indicates the nanocomposites to behave effectively as indirect bandgap semiconductors. The optical bandgap of materials was

calculated by Tauc plot (Fig. S6). The graph between $(\alpha h v)^{1/2}$ *vs hv* and extrapolation of linear slope on the abscissa allowed extraction of the bandgap of the nanocomposite where α is absorption coefficient, h is plank constant and v is the frequency of light. The calculated effective bandgap values for CNF:TNR-2h, CNF:TNR-4h, CNF:TNR-6h and CNF:TNR-8h were found to be 1.52, 1.68, 1.81, and 1.84 eV respectively which clearly demonstrate the visible light absorption capacity of CNF:TNR photocatalyst.

The band alignment in the nanocomposite material is critical for optimal water splitting. In order to obtain more insight into the band edge positions in the CNF:TNR-4h sample, we performed ultraviolet photoelectron spectroscopy (UPS) (Fig. 10). The UPS work function (*WF*) for CNF:TNR-4h sample was calculated by implying the equation $WF = 21.21 - E_{cut\text{-}off}$, where 21.21 eV is the energy of the incident He laser light, and $E_{cut\text{-}off}$ is the cut-off energy. The *WF* value for CNF:TNR-4h was found to be 4.79 eV which is higher than the typically observed WF of bare TiO_2 (4.1-4.3 eV) and indicates the presence of a Type-II (staggered) heterojunction at the embedded CNFQD-TiO_2 interface. The nature of the band-bending at the heterojunction is such as to direct photogenerated electrons toward the TiO_2 and photogenerated holes toward the CNFQDs. The position of the valence band maximum (*VBM*) with respect to the Fermi level was calculated to be -3.32 eV, which can be correlated to +3.51 eV *vs* NHE at pH-0. An additional band edge was observed at 1.29 eV which might originate from the valence band maximum of the CNFQDs suggesting that CNFQDs maintain their distinct individuality in the nanocomposite (Fig. 10b).
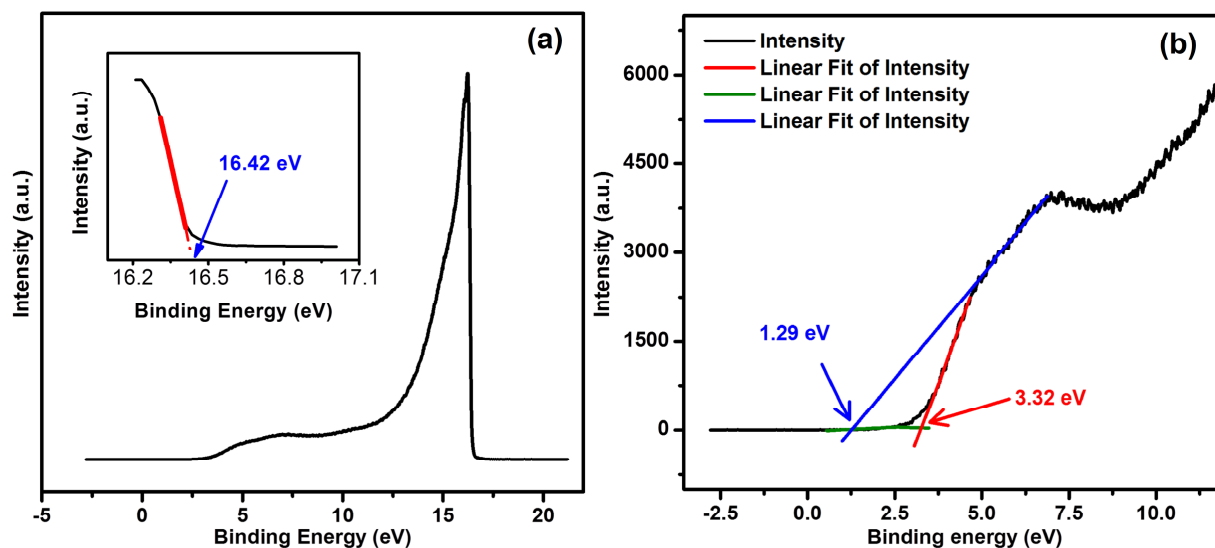
Figure 10. CNF:TNR-4h photocatalyst (a) UPS valence band spectra with inset showing the estimated value of valence band maxima to be 3.32 eV below fermi level; and (b) UPS work function spectra. Inset of (b) shows the estimation of the secondary electron cut-off ($E_{cut-off}$) value. Work function (WF) of 4.79 eV was determined from the UPS work function spectra by using the equation $WF = 21.21 - E_{cut-off}$, where 21.21 eV is energy of the incident He laser used for UPS.

2.3 Photoelectrochemical performance of CNF:TNR nanocomposites

The photoelectrochemical properties of TNR and CNF:TNR samples were determined in a three electrode geometry in 0.1 M KOH electrolyte using CNF:TNR sample grown on FTO as the photoanode, Pt as the cathode/counter-electrode and Ag/AgCl as the reference electrode. The sample photoanode was covered with a surlyn spacer such that a window with an area of 0.3167 cm^2 window was exposed to the solution (to eliminate edge effects). The sample was irradiated with LEDs of different wavelengths, and linear sweep voltammograms were collected for each LED wavelength. The power density at the surface of sample was measured using a calibrated photodiode. For comparison, bare TNR and CNF:TNR samples grown for different durations were tested for photoelectrochemical response at different wavelengths (Fig. 11b). The bare TNR

sample showed a photocurrent of 0.55 mA cm^{-2} at 0.6 V (vs Ag/AgCl) under 365 nm UV irradiation due to the bandgap excitation of TiO$_2$ nanorods followed by oxidative transfer of photogenerated holes to electrolyte species. However, negligible current densities (< 0.01 mA cm^{-2}) were observed for all other tested wavelengths (410-740 nm) for the bare TNR sample as expected due to the poor visible light responsivity of TiO$_2$. All the CNF:TNR samples showed the highest photocurrent density at a wavelength of 425 nm in the visible spectral range. Linear sweep voltammograms of bare TNR and CNF:TNR samples grown for various durations obtained under 425 nm wavelength incident illumination are shown in Fig. 11a. It can be seen in Fig. 11a that the CNF:TNR-4h anode generated the highest photocurrent density (0.18 mA cm^{-2}) at 0.6 V (Fig. 11). In order to probe the photoresponse of the samples, light on-light off experiments were performed using the CNF:TNR-4h sample (Fig. 11c) wherein it can be seen that the sample did not generate a significant current in the dark while a sharp increase in photocurrent was observed under visible light irradiation which clearly demonstrated visible light induced charge separation in the CNFQD-embedded nanorod structure.

We calculated the applied bias photon-to-current efficiency (ABPE) at 425 nm wavelength and plotted the graph of ABPE% *vs* Potential on the RHE scale (Fig. 4d). The ABPE can be calculated by the formula:

ABPE (%) = [J (mA cm^{-2}) x (1.23–V_b)/ P (mW cm^{-2})] x 100 ……………… (1)

where J is the current density, V_b is the applied bias and P is the incident light intensity. The applied voltage on Ag/AgCl scale can be converted to reversible hydrogen electrode (RHE) scale using the following equation.

V_{RHE} = $V_{Ag/AgCl}$ + 0.059 pH + $V^0_{Ag/AgCl}$ …………………………………… (2)
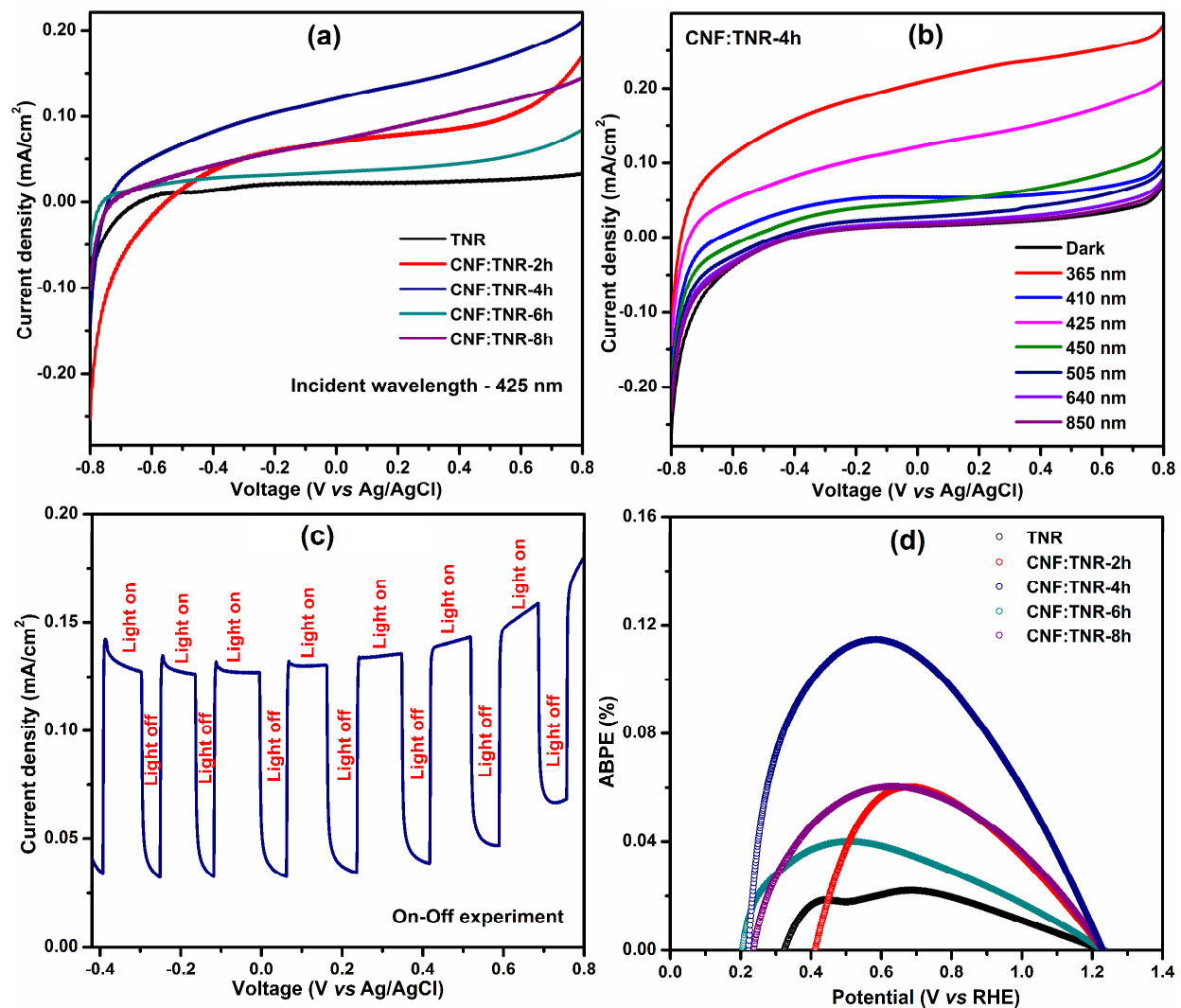
where $V^0_{Ag/AgCl}$ = 0.197 V.

Figure 11. (a) Comparison of photocurrent density at 425 nm wavelength *vs* applied voltage of TNR (black), CNF:TNR-2h (red), CNF:TNR-4h (navy blue), CNF:TNR-6h (dark cyan) and CNF:TNR-8h (purple). (b) Current density *vs* applied voltage graph of CNF:TNR-4h sample at different wavelength, dark (black), 365 (red), 410 (blue), 425 (Magenta), 450 (dark green), 505 (navy blue), 640 (violet) and 850 (purple). (c) Light on-off experiment by using CNF:TNR-4h sample showing visible light (425 nm) response of sample. (d) Plot of ABPE% at 425 nm *vs* Potential at RHE scale of TNR (black), CNF:TNR-2h (red), CNF:TNR-4h (navy blue), CNF:TNR-6h (dark cyan) and CNF:TNR-8h (purple).

We calculated the incident photon-to-current conversion efficiency (IPCE in %) and internal quantum efficiency (IQE in %) of CNF:TNR samples with respect to wavelength (Fig. 11a and 11b). All CNF:TNR samples exhibit maximum quantum yields at an applied bias of 0.4 V *vs* Ag/AgCl and at an incident illumination wavelength of 425 nm (Fig. S7). At 425 nm the internal quantum yields for CNF:TNR-2h, CNF:TNR-4h, CNF:TNR-2h and CNF:TNR-2h samples were found to be 0.56 %, 1.02 %, 0.30 % and 0.71 % respectively.

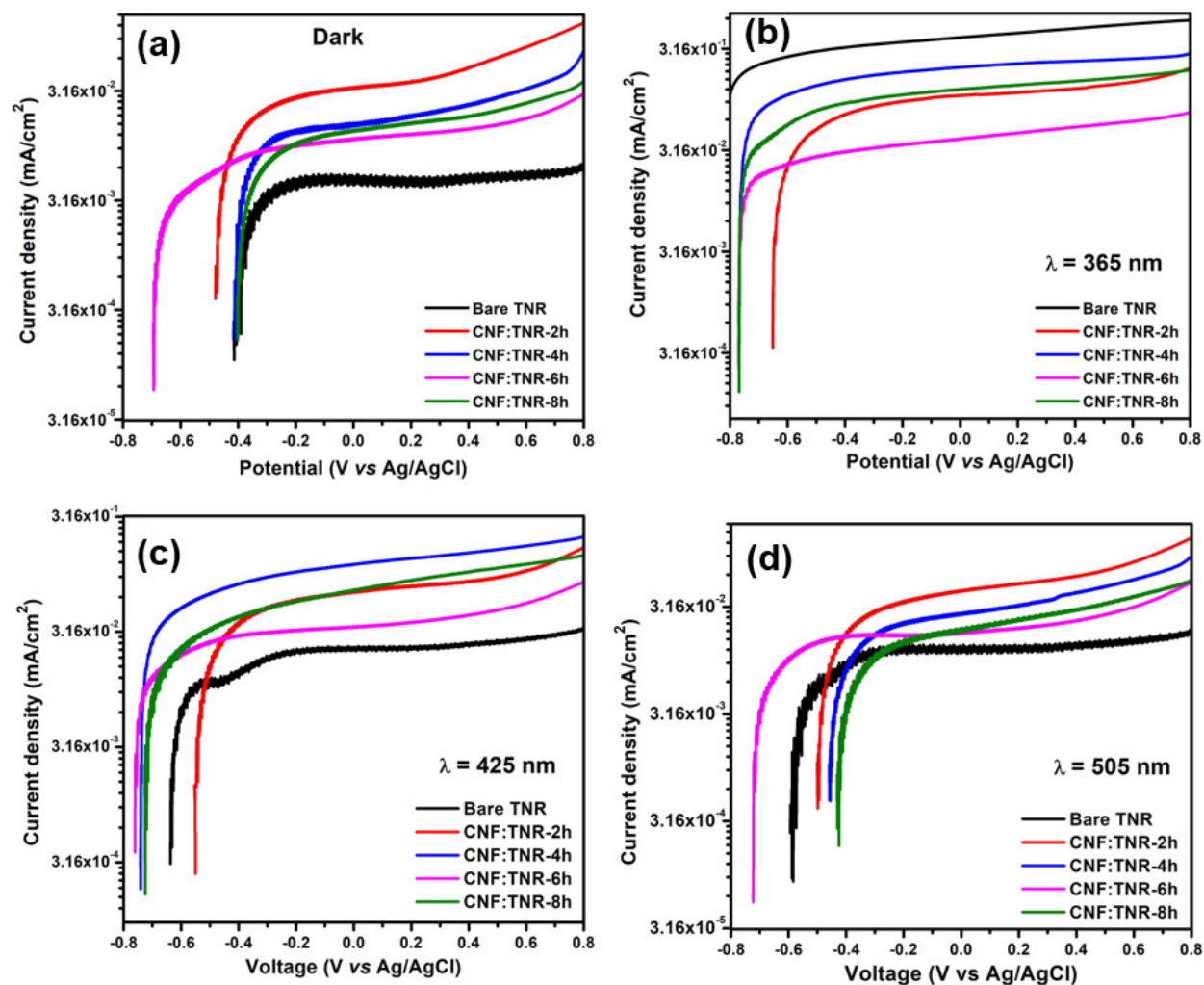## 2.4 Explanation of observed photoelectrochemical behavior

Figure 12. Semilogarithmic photoelectrochemical J-V plots of bare TNR and various CNF:TNR samples, compared under different irradiation conditions (a) Dark (no illumination) (b) Illumination by a 365 nm LED at

an intensity of 42.8 mW cm^{-2} (c) Illumination by a 425 nm LED at an intensity of 47.7 mW cm^{-2} and (d)

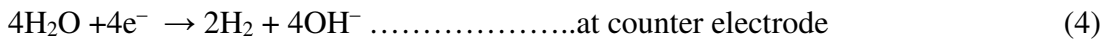Illumination by a 505 nm LED at an intensity of 40.5 mW cm^{-2}.

It can be seen in Fig. 12a that in the dark, the bare TNR sample as well as the CNF:TNR-4h and CNF:TNR-8h samples exhibit a similar open circuit potential (V_{oc}) of ~ −0.4 V vs. Ag/AgCl while the CNF:TNR-2h sample has a V_{oc} that is negatively shifted by ~0.08 V. On the other hand, the CNF:TNR-6h sample has a V_{oc} of ~ −0.7 V in the dark, which is significantly negatively shifted compared to the other samples. Such a large negative shift is indicative of the stronger depletion of electrons at equilibrium in the CNF:TNR-6h sample, which we attribute to the greater *p*-type character of the embedded CNFQDs in the CNF:TNR-6h sample. Greater *p*-type character makes it more favorable for electrons from the CNFQDs to be transferred to the electrolyte instead of holes (desired for a photoanode), and this additional charge transfer channel reduces performance. The CNF:TNR-6h samples also displayed the smallest shifts (less than 0.07 V in absolute terms) in the photocurrent onset potential upon light illumination and generally lower photocurrents (Figs. 12b, 12c and 12d), which is due to significant recombination of electron-hole pairs in this sample. The embedded CNFQDs in the other samples also exhibit slight *p*-type character, which manifests itself in the reduced blocking behavior for electron transfer at the sample-electrolyte interface, and dark current densities that are a factor of 5-10 higher than what is obtained for the bare TNR sample (Fig. 12a).

Light illumination creates a photostationary state in the semiconductor nanocomposite where the open circuit photovoltage is determined by the splitting in the quasi-Fermi levels for electrons and holes [73]. Among the quantum dot embedded nanorod samples, the highest negative shift in V_{oc} of ~ 0.35 V (from -0.40 V to -0.75 V) upon visible light illumination occurs in the CNF:TNR-4h sample (Figs. 12b and 12c). Such a large photo-induced shift in V_{oc} is

indicative of a substantive split in the quasi-Fermi levels for electrons and holes, which provides a large driving force for hole transfer to the electrolyte. The actual realized photocurrent density for the CNF:TNR-4h sample, while being higher than the bare TNR sample by a factor of five, is still low in terms of the quantum yield, suggesting a kinetic limitation in the transfer of holes from CNFQDs to the electrolyte. The two most obvious kinetic limitations are the need for holes in the embedded CNFQDs to tunnel through a thin layer of rutile TiO_2 to reach the electrolyte, and the incomplete wetting of the hydrophobic π-conjugated core of the graphenic CNFQDs by the aqueous electrolyte limiting hole transfer to electrolyte anions. If tunneling were the main hole transfer rate-limiting mechanism, a strong bias dependence of the photocurrent would follow; however the visible light-driven photocurrents for the CNF:TNR samples increase very gently with increasing applied positive bias (Figs. 12b, 12c and 12d), and a bias dependence indicative of tunneling is simply not observed. Therefore, we favor the second explanation related to poor wetting, for the sub-optimal photocurrent densities observed in relation to the V_{oc} shifts obtained under illumination.

On the basis of experimental findings and band positioning, we propose a mechanism of photoelectrochemical water splitting on CNF:TNR samples that is schematically illustrated in Fig. 13. The optical band gap value in the best performing CNF:TNR-4h sample was found to be 1.68 eV from Tauc plot (Fig. S6) which shows that these semiconductor nanocomposites can absorb visible light to generate mobile charge carriers. UPS spectra showed two VBM components at values of -1.29 eV and -3.32 eV *vs* the Fermi level (+1.48 and +3.51 eV *vs* NHE at pH 0) due to presence of CNFQDs and TiO_2. The requirement for efficient water splitting is that the conduction band (CB) position of the semiconductor should be more negative then 0.00 eV *vs* NHE at pH-0 (reduction potential of protons, H^+/H_2) while the valence band position should be more positive

then +1.23 eV *vs* NHE at pH-0 (oxidation potention of water H_2O/O_2). From UPS spectra, the VB position of TiO_2 in CNF:TNR was found to be +3.51 eV, which was more oxidative than VB potential of TiO_2 (+2.94 eV) which renders the nanocomposite more oxidative to facilitate water oxidation. Photogenerated electrons in the LUMO/CB of CNFQDs are transferred to the CB of TiO_2 due to energetic offset [74, 75], and a significant fraction of photogenerated holes in the VB of TiO_2 are transferred to the HOMO/VB of the CNFQDs (instead of transferring directly to the electrolyte anions). This inference was supported by the decreased photocurrents obtained using CNF:TNR nanocomposites under ultraviolet illumination by 365 nm photons (Fig. 12b) when both the TiO_2 and CNFQDs are photoexcited as opposed to the significantly higher photoelectrochemical activity of CNF:TNR nanocomposites under visible light illumination (Fig. 12c and Fig. 12d) when the CNFQDs alone are excited. This inference is also in accordance with the decrease in PL intensity (Fig. 8b) and decrease in PL lifetime (Fig. 9) in the CNFQD-embedded nanorods. The electrons injected into the conduction band of TiO_2 were extracted by FTO anode and supplied to Pt cathode where they are consumed to reduce protons.
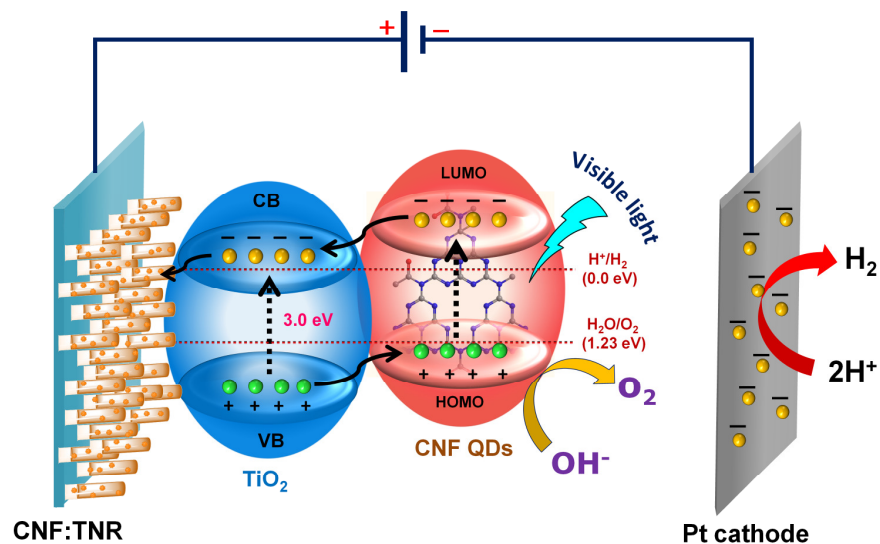
$$4OH^- + 4h^+ \rightarrow O_2 + 2H_2O \quad \ldots\ldots\ldots\ldots\ldots\ldots\text{at anode} \tag{3}$$

$$4H_2O + 4e^- \rightarrow 2H_2 + 4OH^- \quad \ldots\ldots\ldots\ldots\ldots\text{at counter electrode} \tag{4}$$

Figure 13. Possible reaction mechanism of water splitting over CNF:TNR photocatalyst

2.5 Photoelectrochemical stability and re-usability of CNF:TNR nanocomposites

In order to investigate the long term usability and consistency of the photoresponse behaviour, we performed five re-use experiments on CNF:TNR-4h sample. For the re-use experiment after each cycle, the "used" sample was washed with DI water and dried at 100 ℃. The re-use experiments showed no significant change in photoresponse of CNF:TNR samples, which confirmed the durability of the CNF:TNR samples for long term application (Fig. 14). After performing photoelectrochemical measurements, the "used" CNF:TNR-4h sample was photographed using a digital camera and its morphology was examined again in the FESEM (Fig. 15); the imaging confirmed that there was almost no degradation in either the color or the internal morphology of the samples following multiple re-use cycles. In addition, the "used" CNF:TNR-4h sample was also analysed with XRD, Raman, UV-Vis, FTIR, PL spectroscopies and the collected spectra were compared with a freshly synthesized sample – these measurements validated the robustness and photostability of the photocatalyst (Fig. 16). The spectra were similar to freshly prepared samples

which clearly indicates that after multiple photoelectrochemical cycles, the CNF:TNR photocatalyst remains intact with its chemical, optical and structural properties unchanged.
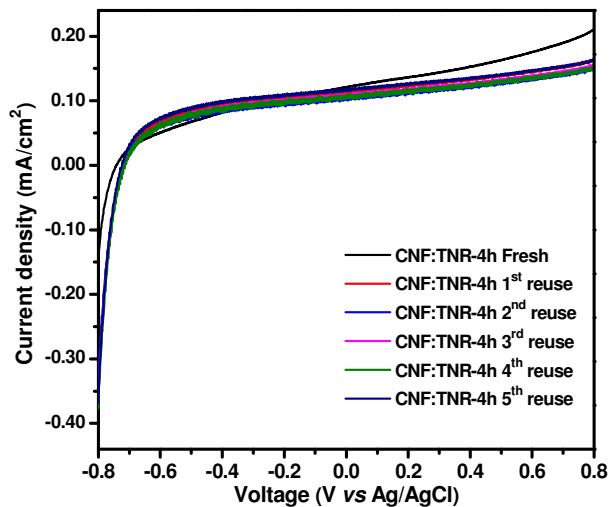

Figure 14. Photoelectrochemical water splitting results by using CNF:TNR-4h resued sample at different wavelength. Fresh sample (black), first reused (red), second reused (blue), third reused (magenta), fourth reused (olive green), and fifth reused (navy blue).
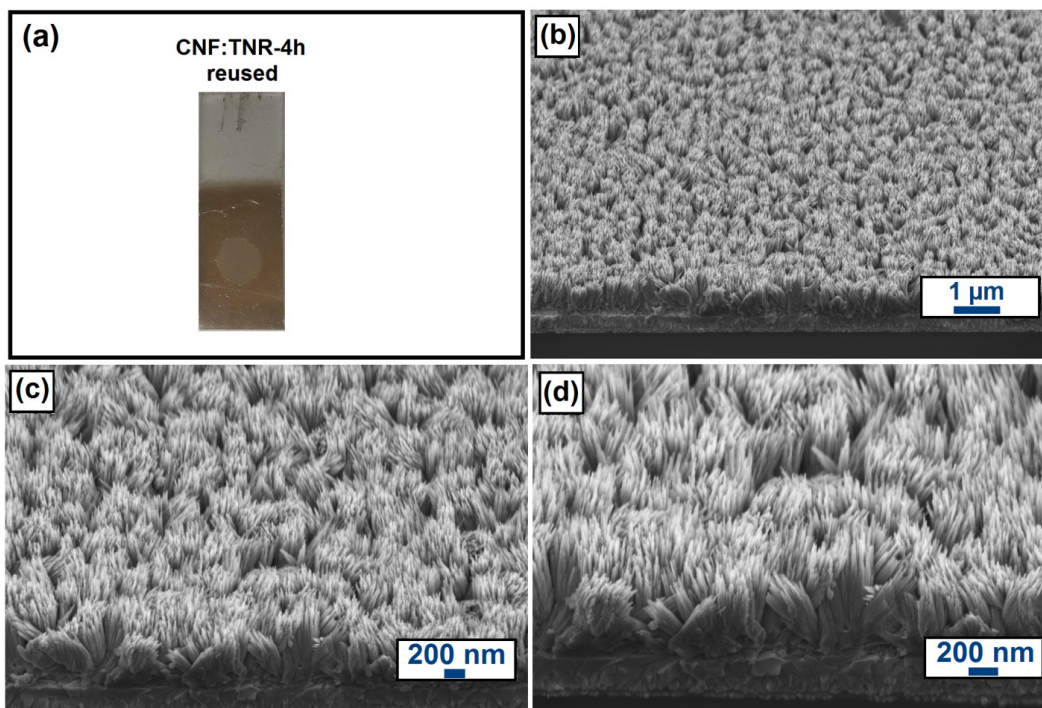
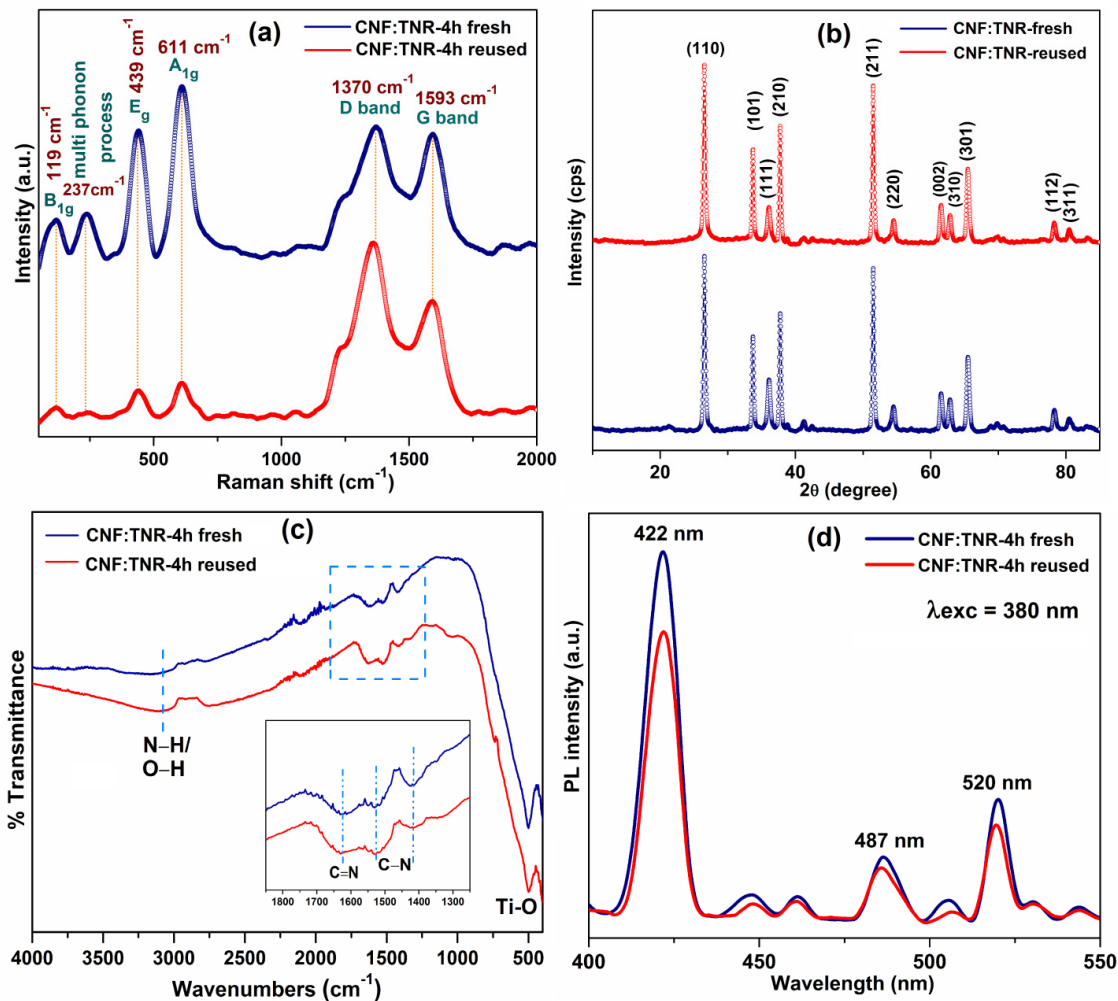**Figure 15**. (a) Photograph of CNF:TNR-4h reused sample and (b-d) FE-SEM image of reused CNF:TNR-4h sample.

Figure 16. (a) Raman spectra, (b) X-ray diffractogram, (c) FTIR spectra; Inset show expanded region between 1250 cm^{-1} to 1850 cm^{-1} (d) PL spectra of CNF:TNR-4h fresh sample (navy blue) and "used" sample (red).

3. Conclusion

The family of carbonaceous quantum dots is expanding everyday as new compositions and applications are being developed. We report the successful synthesis of fluorine doped carbon nitride quantum dots (CNFQDs) by solid-state reaction for the first time. CNFQDs were found to be highly fluorescent with a bright blue emission peaking at 417-422 nm. The direct application

of CNFQDs in photoelectrochemical water-splitting is limited by the need for an *n*-type semiconducting scaffold and the tendency of the carbon nitride quantum dots to leach out in aqueous electrolytes. In response, we used an *in situ* hydrothermal process to embed CNFQDs inside rutile-phase TiO_2 nanorods (TNRs). Encasing of the CNFQDs in a TiO_2 matrix prevented them from leaching out into the electrolyte. Photoelectrochemical measurements indicated a strong visible light induced photoresponse in the CNFQD-embedded TNRs that extended up to 500 nm. The best performing CNF:TNR-4h samples produced photocurrent densities greater than in bare TNRs by a factor of five at visible wavelengths while producing open circuit photovoltages as high as -0.76 V *vs* Ag/AgCl. A combination of steady-state and time-resolved PL studies, photoelectrochemical data analysis and UPS spectra were used to infer efficient charge separation at the TiO_2-CNFQD hetero-interface following visible light photoexcitation. A remarkable result was the observation of exceptional photostability and consistency of photoresponse of the CNF-TNR nanocomposites after multiple re-use cycles, which was confirmed by optoelectronic, structural and spectroscopic characterization. Although the electronic properties of the CNFQD-TiO_2-electrolyte heterojunction require further optimization to improve hole transfer to electrolyte anions, the demonstration of superior photostability and photoresponsivity to visible light points to a viable route forward to construct high performance photocatalysts based on one dimensional TiO_2 nanostructures sensitized by graphenic quantum dots.

Conflict of interest statement

The authors have no conflicts to declare.

Authors contributions

PK and UKT synthesized and characterized the materials and performed water splitting experiments. PK interpreted the characterization data and was involved in writing the manuscript writing. KA helped in characterization and data collection. PK was responsible for collecting and analyzing the XPS data, UPS data and electrochemical data. RK performed HR-TEM analysis of samples. SZ assisted with LED calibration and intensity measurements. SP assisted with catalyst synthesis and optimization. KS supervised the research and edited the manuscript.

References

[1] Y. Tachibana, L. Vayssieres, J.R. Durrant, Artificial photosynthesis for solar water-splitting, Nature Photonics 6(8) (2012) 511-518.
[2] N.S. Lewis, D.G. Nocera, Powering the planet: Chemical challenges in solar energy utilization, Proceedings of the National Academy of Sciences 103(43) (2006) 15729-15735.
[3] K.S. Joya, Y.F. Joya, K. Ocakoglu, R. van de Krol, Water-Splitting Catalysis and Solar Fuel Devices: Artificial Leaves on the Move, Angewandte Chemie International Edition 52(40) (2013) 10426-10437.
[4] A. Kudo, Y. Miseki, Heterogeneous photocatalyst materials for water splitting, Chemical Society Reviews 38(1) (2009) 253-278.
[5] T. Hisatomi, J. Kubota, K. Domen, Recent advances in semiconductors for photocatalytic and photoelectrochemical water splitting, Chemical Society Reviews 43(22) (2014) 7520-7535.
[6] D. Chen, X. Zhang, A.F. Lee, Synthetic strategies to nanostructured photocatalysts for CO 2 reduction to solar fuels and chemicals, Journal of Materials Chemistry A 3(28) (2015) 14487-14516.

[7] G. Wang, H. Wang, Y. Ling, Y. Tang, X. Yang, R.C. Fitzmorris, C. Wang, J.Z. Zhang, Y. Li, Hydrogen-treated TiO_2 nanowire arrays for photoelectrochemical water splitting, Nano Lett. 11(7) (2011) 3026-3033.

[8] Y. Tang, Y. Su, N. Yang, L. Zhang, Y. Lv, Carbon nitride quantum dots: a novel chemiluminescence system for selective detection of free chlorine in water, Analytical chemistry 86(9) (2014) 4528-4535.

[9] X. Chen, Q. Liu, Q. Wu, P. Du, J. Zhu, S. Dai, S. Yang, Incorporating Graphitic Carbon Nitride (g-C3N4) Quantum Dots into Bulk-Heterojunction Polymer Solar Cells Leads to Efficiency Enhancement, Advanced Functional Materials 26(11) (2016) 1719-1728.

[10] V. Kumar, S. Arora, S. Kumar, T.W. Kang, H.C. Jeon, Annealing led conversion from polypyrrole to carbon nitride nanowires and the fabrication of highly efficient ammonia sensing device, Journal of Materials Science-Materials in Electronics 28(23) (2017) 17791-17797.

[11] M. Mousavi, A. Habibi-Yangjeh, S.R. Pouran, Review on magnetically separable graphitic carbon nitride-based nanocomposites as promising visible-light-driven photocatalysts, Journal of Materials Science-Materials in Electronics 29(3) (2018) 1719-1747.

[12] H. Zhang, Y. Chen, M. Liang, L. Xu, S. Qi, H. Chen, X. Chen, Solid-phase synthesis of highly fluorescent nitrogen-doped carbon dots for sensitive and selective probing ferric ions in living cells, Analytical chemistry 86(19) (2014) 9846-9852.

[13] Y.-C. Lu, J. Chen, A.-J. Wang, N. Bao, J.-J. Feng, W. Wang, L. Shao, Facile synthesis of oxygen and sulfur co-doped graphitic carbon nitride fluorescent quantum dots and their application for mercury (II) detection and bioimaging, Journal of Materials Chemistry C 3(1) (2015) 73-78.

[14] Y. Wang, Y. Di, M. Antonietti, H. Li, X. Chen, X. Wang, Excellent visible-light photocatalysis of fluorinated polymeric carbon nitride solids, Chemistry of Materials 22(18) (2010) 5119-5121.

[15] N. Wang, H. Fan, J. Sun, Z. Han, J. Dong, S. Ai, Fluorine-doped carbon nitride quantum dots: Ethylene glycol-assisted synthesis, fluorescent properties, and their application for bacterial imaging, Carbon 109 (2016) 141-148.

[16] S.N. Habisreutinger, L. Schmidt-Mende, J.K. Stolarczyk, Photocatalytic reduction of CO_2 on TiO_2 and other semiconductors, Angewandte Chemie International Edition 52(29) (2013) 7372-7408.

[17] X. Zhang, F. Han, B. Shi, S. Farsinezhad, G.P. Dechaine, K. Shankar, Photocatalytic Conversion of Diluted CO_2 into Light Hydrocarbons Using Periodically Modulated Multiwalled Nanotube Arrays, Angewandte Chemie International Edition (2012) n/a-n/a.

[18] S. Farsinezhad, H. Sharma, K. Shankar, Interfacial band alignment for photocatalytic charge separation in TiO_2 nanotube arrays coated with CuPt nanoparticles, Physical Chemistry Chemical Physics 17(44) (2015) 29723-29733.

[19] R.S. Dhabbe, A.N. Kadam, M.B. Suwarnkar, M.R. Kokate, K.M. Garadkar, Enhancement in the photocatalytic activity of Ag loaded N-doped TiO_2 nanocomposite under sunlight, Journal of Materials Science-Materials in Electronics 25(7) (2014) 3179-3189.

[20] V. Krishnakumar, S. Boobas, J. Jayaprakash, M. Rajaboopathi, B. Han, M. Louhi-Kultanen, Effect of Cu doping on TiO_2 nanoparticles and its photocatalytic activity under visible light, Journal of Materials Science-Materials in Electronics 27(7) (2016) 7438-7447.

[21] K. Trabelsi, A. Hajjaji, I. Ka, M. Gaidi, B. Bessais, M.A. El Khakani, Optoelectronic and photocatalytic properties of in situ platinum-doped TiO_2 films deposited by means of pulsed laser ablation technique, Journal of Materials Science-Materials in Electronics 28(4) (2017) 3317-3324.

[22] H. Wang, J. Lewis, Second-generation photocatalytic materials: anion-doped TiO2, Journal of Physics: Condensed Matter 18(2) (2005) 421.

[23] T. Ohno, M. Akiyoshi, T. Umebayashi, K. Asai, T. Mitsui, M. Matsumura, Preparation of S-doped TiO2 photocatalysts and their photocatalytic activities under visible light, Applied Catalysis A: General 265(1) (2004) 115-121.

[24] K. Yang, Y. Dai, B. Huang, M.-H. Whangbo, Density Functional Characterization of the Visible-Light Absorption in Substitutional C-Anion- and C-Cation-Doped TiO2, The Journal of Physical Chemistry C 113(6) (2009) 2624-2629.

[25] K. Shankar, K.C. Tep, G.K. Mor, C.A. Grimes, An electrochemical strategy to incorporate nitrogen in nanostructured TiO2 thin films: modification of bandgap and photoelectrochemical properties, Journal of Physics D-Applied Physics 39(11) (2006) 2361-2366.

[26] H.L. Hou, F.M. Gao, M.H. Shang, L. Wang, J.J. Zheng, Q. Liu, Z.B. Yang, J.H. Xu, W.Y. Yang, Enhanced visible-light responsive photocatalytic activity of N-doped TiO2 thoroughly mesoporous nanofibers, Journal of Materials Science-Materials in Electronics 28(4) (2017) 3796-3805.

[27] H.Y. Cheong, S.Y. Kim, Y.J. Cho, D.W. Cho, C.H. Kim, H.J. Son, C. Pac, S.O. Kang, Photosensitization Behavior of 1011) Complexes in Selective Reduction of CO2 by Re(I)-Complex-Anchored TiO2 Hybrid Catalyst, Inorganic Chemistry 56(19) (2017) 12042-12053.

[28] E. Bae, W. Choi, J. Park, H.S. Shin, S.B. Kim, J.S. Lee, Effects of Surface Anchoring Groups (Carboxylate vs Phosphonate) in Ruthenium-Complex-Sensitized TiO2 on Visible Light Reactivity in Aqueous Suspensions, The Journal of Physical Chemistry B 108(37) (2004) 14093-14101.

[29] J. Zhang, P. Du, J. Schneider, P. Jarosz, R. Eisenberg, Photogeneration of Hydrogen from Water Using an Integrated System Based on TiO2 and Platinum(II) Diimine Dithiolate Sensitizers, Journal of the American Chemical Society 129(25) (2007) 7726-7727.

[30] H. Zhu, B. Yang, J. Xu, Z. Fu, M. Wen, T. Guo, S. Fu, J. Zuo, S. Zhang, Construction of Z-scheme type CdS–Au–TiO2 hollow nanorod arrays with enhanced photocatalytic activity, Applied Catalysis B: Environmental 90(3) (2009) 463-469.

[31] Y. Zhao, X. Huang, X. Tan, T. Yu, X.L. Li, L.B. Yang, S.C. Wang, Fabrication of BiOBr nanosheets@TiO2 nanobelts p-n junction photocatalysts for enhanced visible-light activity, Applied Surface Science 365 (2016) 209-217.

[32] A. Naldoni, M. Allieta, S. Santangelo, M. Marelli, F. Fabbri, S. Cappelli, C.L. Bianchi, R. Psaro, V. Dal Santo, Effect of Nature and Location of Defects on Bandgap Narrowing in Black TiO2 Nanoparticles, Journal of the American Chemical Society 134(18) (2012) 7600-7603.

[33] W. Zhou, W. Li, J.Q. Wang, Y. Qu, Y. Yang, Y. Xie, K.F. Zhang, L. Wang, H.G. Fu, D.Y. Zhao, Ordered Mesoporous Black TiO2 as Highly Efficient Hydrogen Evolution Photocatalyst, Journal of the American Chemical Society 136(26) (2014) 9280-9283.

[34] G.K. Mor, K. Shankar, M. Paulose, O.K. Varghese, C.A. Grimes, Use of highly-ordered TiO2 nanotube arrays in dye-sensitized solar cells, Nano Lett. 6(2) (2006) 215-218.

[35] P.D. Tran, L.H. Wong, J. Barber, J.S. Loo, Recent advances in hybrid photocatalysts for solar fuel production, Energy & Environmental Science 5(3) (2012) 5902-5918.

[36] S. Liu, J. Yu, M. Jaroniec, Tunable photocatalytic selectivity of hollow TiO2 microspheres composed of anatase polyhedra with exposed {001} facets, Journal of the American Chemical Society 132(34) (2010) 11914-11916.

[37] V. Aroutiounian, V. Arakelyan, G. Shahnazaryan, G. Stepanyan, J.A. Turner, S.S. Kocha, Investigations of the Fe 1.99 Ti 0.01 O 3–electrolyte interface, Electrochimica Acta 45(12) (2000) 1999-2005.

[38] P. Kar, Y. Zhang, N. Mahdi, U.K. Thakur, B.D. Wiltshire, R. Kisslinger, K. Shankar, Heterojunctions of mixed phase TiO2 nanotubes with Cu, CuPt, and Pt nanoparticles: interfacial band alignment and visible light photoelectrochemical activity, Nanotechnology 29(1) (2017) 014002.

[39] P. Kar, S. Farsinezhad, N. Mahdi, Y. Zhang, U. Obuekwe, H. Sharma, J. Shen, N. Semagina, K. Shankar, Enhanced CH4 yield by photocatalytic CO2 reduction using TiO2 nanotube arrays grafted with Au, Ru, and ZnPd nanoparticles, Nano Research 9(11) (2016) 3478-3493.

[40] B. Liu, E.S. Aydil, Growth of oriented single-crystalline rutile TiO2 nanorods on transparent conducting substrates for dye-sensitized solar cells, Journal of the American Chemical Society 131(11) (2009) 3985-3990.

[41] H.-S. Kim, J.-W. Lee, N. Yantara, P.P. Boix, S.A. Kulkarni, S. Mhaisalkar, M. Grätzel, N.-G. Park, High efficiency solid-state sensitized solar cell-based on submicrometer rutile TiO2 nanorod and CH3NH3PbI3 perovskite sensitizer, Nano Lett. 13(6) (2013) 2412-2417.

[42] X.J. Feng, K. Zhu, A.J. Frank, C.A. Grimes, T.E. Mallouk, Rapid Charge Transport in Dye-Sensitized Solar Cells Made from Vertically Aligned Single-Crystal Rutile TiO2 Nanowires, Angew. Chem.-Int. Edit. 51(11) (2012) 2727-2730.

[43] X. Sheng, D.Q. He, J. Yang, K. Zhu, X.J. Feng, Oriented Assembled TiO2 Hierarchical Nanowire Arrays with Fast Electron Transport Properties, Nano Lett. 14(4) (2014) 1848-1852.

[44] A. Mohammadpour, P. Kar, B.D. Wiltshire, A.M. Askar, K. Shankar, Electron Transport, Trapping and Recombination in Anodic TiO$_2$ Nanotube Arrays, Current Nanoscience 11(5) (2015) 593-614.

[45] X. Sheng, L.P. Chen, T. Xu, K. Zhu, X.J. Feng, Understanding and removing surface states limiting charge transport in TiO2 nanowire arrays for enhanced optoelectronic device performance, Chem. Sci. 7(3) (2016) 1910-1913.

[46] A. Mohammadpour, B.D. Wiltshire, Y. Zhang, S. Farsinezhad, A.M. Askar, R. Kisslinger, Y. Ren, P. Kar, K. Shankar, 100-fold improvement in carrier drift mobilities in alkanephosphonate-passivated monocrystalline TiO 2 nanowire arrays, Nanotechnology 28(14) (2017) 144001.

[47] J. Pan, Y. Sheng, J. Zhang, J. Wei, P. Huang, X. Zhang, B. Feng, Preparation of carbon quantum dots/TiO 2 nanotubes composites and their visible light catalytic applications, Journal of Materials Chemistry A 2(42) (2014) 18082-18086.

[48] J. Su, L. Zhu, P. Geng, G. Chen, Self-assembly graphitic carbon nitride quantum dots anchored on TiO 2 nanotube arrays: an efficient heterojunction for pollutants degradation under solar light, Journal of hazardous materials 316 (2016) 159-168.

[49] J. Su, L. Zhu, G. Chen, Ultrasmall graphitic carbon nitride quantum dots decorated self-organized TiO 2 nanotube arrays with highly efficient photoelectrochemical activity, Applied Catalysis B: Environmental 186 (2016) 127-135.

[50] X.-j. Wang, W.-y. Yang, F.-t. Li, Y.-b. Xue, R.-h. Liu, Y.-j. Hao, In situ microwave-assisted synthesis of porous N-TiO2/g-C3N4 heterojunctions with enhanced visible-light photocatalytic properties, Industrial & Engineering Chemistry Research 52(48) (2013) 17140-17150.

[51] P. Kumar, C. Joshi, N. Labhsetwar, R. Boukherroub, S.L. Jain, A novel Ru/TiO 2 hybrid nanocomposite catalyzed photoreduction of CO 2 to methanol under visible light, Nanoscale 7(37) (2015) 15258-15267.

[52] S. Chen, N. Hao, D. Jiang, X. Zhang, Z. Zhou, Y. Zhang, K. Wang, Graphitic carbon nitride quantum dots in situ coupling to Bi 2 MoO 6 nanohybrids with enhanced charge transfer performance and photoelectrochemical detection of copper ion, Journal of Electroanalytical Chemistry 787 (2017) 66-71.

[53] J. Fu, B. Chang, Y. Tian, F. Xi, X. Dong, Novel C 3 N 4–CdS composite photocatalysts with organic–inorganic heterojunctions: in situ synthesis, exceptional activity, high stability and photocatalytic mechanism, Journal of Materials Chemistry A 1(9) (2013) 3083-3090.

[54] C. Han, Y. Wang, Y. Lei, B. Wang, N. Wu, Q. Shi, Q. Li, In situ synthesis of graphitic-C3N4 nanosheet hybridized N-doped TiO2 nanofibers for efficient photocatalytic H2 production and degradation, Nano Research 8(4) (2015) 1199-1209.

[55] J. Zhou, Y. Yang, C.-y. Zhang, A low-temperature solid-phase method to synthesize highly fluorescent carbon nitride dots with tunable emission, Chemical Communications 49(77) (2013) 8605-8607.

[56] S. Liu, J. Tian, L. Wang, Y. Luo, J. Zhai, X. Sun, Preparation of photoluminescent carbon nitride dots from CCl4 and 1, 2-ethylenediamine: a heat-treatment-based strategy, Journal of Materials Chemistry 21(32) (2011) 11726-11729.

[57] W. Wang, C.Y. Jimmy, Z. Shen, D.K. Chan, T. Gu, gC 3 N 4 quantum dots: direct synthesis, upconversion properties and photocatalytic application, Chemical Communications 50(70) (2014) 10148-10150.

[58] S. Barman, M. Sadhukhan, Facile bulk production of highly blue fluorescent graphitic carbon nitride quantum dots and their application as highly selective and sensitive sensors for the detection of mercuric and iodide ions in aqueous media, Journal of Materials Chemistry 22(41) (2012) 21832-21837.

[59] A. Kumar, P. Kumar, C. Joshi, S. Ponnada, A.K. Pathak, A. Ali, B. Sreedhar, S.L. Jain, A [Fe (bpy) 3] 2+ grafted graphitic carbon nitride hybrid for visible light assisted oxidative coupling of benzylamines under mild reaction conditions, Green Chemistry 18(8) (2016) 2514-2521.

[60] H. Wang, Y. Bai, Q. Wu, W. Zhou, H. Zhang, J. Li, L. Guo, Rutile TiO2 nano-branched arrays on FTO for dye-sensitized solar cells, Physical Chemistry Chemical Physics 13(15) (2011) 7008-7013.

[61] P. Kar, Y. Zhang, S. Farsinezhad, A. Mohammadpour, B.D. Wiltshire, H. Sharma, K. Shankar, Rutile phase n-and p-type anodic titania nanotube arrays with square-shaped pore morphologies, Chemical Communications 51(37) (2015) 7816-7819.

[62] Y. Zhang, C.X. Harris, P. Wallenmeyer, J. Murowchick, X. Chen, Asymmetric lattice vibrational characteristics of rutile TiO2 as revealed by laser power dependent Raman spectroscopy, The Journal of Physical Chemistry C 117(45) (2013) 24015-24022.

[63] J.-G. Li, T. Ishigaki, X. Sun, Anatase, brookite, and rutile nanocrystals via redox reactions under mild hydrothermal conditions: phase-selective synthesis and physicochemical properties, The Journal of Physical Chemistry C 111(13) (2007) 4969-4976.

[64] Z. Xu, H. Li, Z. Wu, J. Sun, Z. Ying, J. Wu, N. Xu, Enhanced charge separation of vertically aligned CdS/gC 3 N 4 heterojunction nanocone arrays and corresponding mechanisms, Journal of Materials Chemistry C 4(31) (2016) 7501-7507.

[65] M.S. Dresselhaus, A. Jorio, M. Hofmann, G. Dresselhaus, R. Saito, Perspectives on carbon nanotubes and graphene Raman spectroscopy, Nano Lett. 10(3) (2010) 751-758.

[66] Z. Song, T. Lin, L. Lin, S. Lin, F. Fu, X. Wang, L. Guo, Invisible Security Ink Based on Water-Soluble Graphitic Carbon Nitride Quantum Dots, Angewandte Chemie International Edition 55(8) (2016) 2773-2777.

[67] Q. Lin, L. Li, S. Liang, M. Liu, J. Bi, L. Wu, Efficient synthesis of monolayer carbon nitride 2D nanosheet with tunable concentration and enhanced visible-light photocatalytic activities, Applied Catalysis B: Environmental 163 (2015) 135-142.

[68] E.Z. Lee, Y.S. Jun, W.H. Hong, A. Thomas, M.M. Jin, Cubic Mesoporous Graphitic Carbon (IV) Nitride: An All-in-One Chemosensor for Selective Optical Sensing of Metal Ions, Angewandte Chemie International Edition 49(50) (2010) 9706-9710.

[69] Y. Yang, G. Liu, J.T. Irvine, H.M. Cheng, Enhanced Photocatalytic H2 Production in Core–Shell Engineered Rutile TiO2, Advanced Materials 28(28) (2016) 5850-5856.

[70] A. Tiwari, I. Mondal, S. Ghosh, N. Chattopadhyay, U. Pal, Fabrication of mixed phase TiO 2 heterojunction nanorods and their enhanced photoactivities, Physical Chemistry Chemical Physics 18(22) (2016) 15260-15268.

[71] T. Ji, Z. Cui, W. Zhang, Y. Cao, Y. Zhang, S.-a. He, M. Xu, Y. Sun, R. Zou, J. Hu, UV and visible light synergetic photodegradation using rutile TiO 2 nanorod arrays based on ap–n Junction, Dalton Transactions 46(13) (2017) 4296-4302.

[72] A. Amtout, R. Leonelli, Optical properties of rutile near its fundamental band gap, Physical Review B 51(11) (1995) 6842-6851.

[73] M.G. Walter, E.L. Warren, J.R. McKone, S.W. Boettcher, Q. Mi, E.A. Santori, N.S. Lewis, Solar Water Splitting Cells, Chemical Reviews 110(11) (2010) 6446-6473.

[74] P. Kar, S. Farsinezhad, X. Zhang, K. Shankar, Anodic Cu2S and CuS nanorod and nanowall arrays: preparation, properties and application in CO2 photoreduction, Nanoscale 6(23) (2014) 14305-14318.

[75] M. Reli, P. Huo, M. Šihor, N. Ambrožová, I. Troppová, L. Matějová, J. Lang, L. Svoboda, P. Kuśtrowski, M. Ritz, P. Praus, K. Kočí, Novel TiO2/C3N4 Photocatalysts for Photocatalytic Reduction of CO2 and for Photocatalytic Decomposition of N2O, The Journal of Physical Chemistry A 120(43) (2016) 8564-8573.